Title

High-density transparent graphene arrays for predicting cellular calcium activity at depth from surface potential recordings

Authors

Ramezani, Mehrdad

Kim, Jeong-Hoon

Liu, Xin

et al.

Peer reviewed

High-density transparent graphene arrays for predicting cellular calcium activity at depth from surface potential recordings

Mehrdad Ramezani[1,4], **Jeong-Hoon Kim**[1,4], **Xin Liu**[1], **Chi Ren**[2], **Abdullah Alothman**[1], **Chawina De-Eknamkul**[3], **Madison N. Wilson**[1], **Ertugrul Cubukcu**[3], **Vikash Gilja**[1], **Takaki Komiyama**[2], **Duygu Kuzum**[1,✉]

[1]Department of Electrical and Computer Engineering, University of California San Diego, La Jolla, CA, USA.

[2]Department of Neurosciences, University of California San Diego, La Jolla, CA, USA.

[3]Department of NanoEngineering, University of California San Diego, La Jolla, CA, USA.

[4]These authors contributed equally: Mehrdad Ramezani, Jeong-Hoon Kim.

Abstract

Optically transparent neural microelectrodes have facilitated simultaneous electrophysiological recordings from the brain surface with the optical imaging and stimulation of neural activity. A remaining challenge is to scale down the electrode dimensions to the single-cell size and increase the density to record neural activity with high spatial resolution across large areas to capture nonlinear neural dynamics. Here we developed transparent graphene microelectrodes with ultrasmall openings and a large, transparent recording area without any gold extensions in the field of view with high-density microelectrode arrays up to 256 channels. We used platinum nanoparticles to overcome the quantum capacitance limit of graphene and to scale down the microelectrode diameter to 20 μm. An interlayer-doped double-layer graphene was introduced to prevent open-circuit failures. We conducted multimodal experiments, combining the recordings of cortical potentials of microelectrode arrays with two-photon calcium imaging of the mouse visual cortex. Our results revealed that visually evoked responses are spatially localized for high-

frequency bands, particularly for the multiunit activity band. The multiunit activity power was found to be correlated with cellular calcium activity. Leveraging this, we employed dimensionality reduction techniques and neural networks to demonstrate that single-cell and average calcium activities can be decoded from surface potentials recorded by high-density transparent graphene arrays.

Understanding the complex dynamics of the brain and the central nervous system require the study of mechanisms and functions in a diverse set of spatial and temporal scales[1,2]. Spatial scales encompass neural circuits in millimetres or centimetres, single neurons in micrometres, synapses in submicrometres and proteins such as ion channels and receptors at the nanoscale. This spatial diversity also cultivates temporal diversity where some molecular processes are taking place in microseconds, action potentials in sub-milliseconds, neurotransmitter or hormone release in minutes to hours and learning and behavioural changes in hours to days[1]. Monitoring neural dynamics and interrogating neural functions across these diverse spatial and temporal scales is not possible using a single tool or technology. Therefore, the integration of multiple tools in the same experiment have been widely employed to link mechanisms and functions operating at these different spatiotemporal scales towards a more comprehensive understanding of the brain.

To date, multimodal experiments have been used to investigate neural dynamics with applications ranging from studies of neural circuits[3–5] or pathophysiology of brain disorders[6,7] to hybrid brain–computer interfaces[8,9]. Among these multimodal approaches, experiments concurrently recording electrophysiological responses during optical imaging and optogenetic stimulation have become a powerful approach to (1) combine the temporal resolution advantage of electrophysiology with the high spatial resolution and cell-type specificity of optical methods, (2) to bridge the knowledge gap between basic neuroscience research relying on optical methods employing genetic modifications and clinical research mainly using electrical recordings, (3) to expand the spatial reach of neural recordings[10] and (4) to identify cell types through opto-tagging during the electrophysiological recordings of neuronal spikes[11]. To enable a crosstalk- and artefact-free integration of electrical and optical modalities, numerous transparent microelectrode technologies have been developed based on different materials including graphene[12–16], indium tin oxide[17–20], carbon nanotube meshes[21], metal nanowires[22–24], meshes or grids[25–27] and PEDOT:PSS[28–31]. These devices, however, have limitations such as large electrode opening sizes (50 μm or larger), low channel counts (maximum, 16) and limited coverage (maximum, 3.6 mm^2), restricting the spatiotemporal resolution for neural recordings. Reducing the electrode dimensions to the single-cell size, for instance, is desirable to detect high-frequency activity including multiunit activity (MUA) and single-unit activity with a high signal-to-noise ratio[32]. Increasing the array density and channel count is also essential to capture the neural dynamics with high spatial resolution across large areas[33,34]. Moreover, there are several other constraints that limit the use of these technologies as multimodal chronic interfaces (Extended Data Table 1 and Supplementary Discussion 1)[23,28].

Within the spectrum of materials, graphene offers characteristics desirable for multimodal neural interfaces including transparency, artefact-free recording capability[12,14], flexibility[35],

low noise[36], biocompatibility[37] and chronic reliability[38–40]. Furthermore, active neural interfaces based on graphene have been shown to offer exceptional bandwidth by recording ultraslow neural dynamics without voltage drift[41,42]. To realize high-density transparent graphene arrays with ultrasmall electrodes, however, two important challenges remain to be addressed. (1) To keep the field of view (FoV) clear, microwires of the arrays need to be completely transparent, particularly for high-density arrays with thin and long graphene wires. However, scaling the graphene wires results in increased wire resistance (leading to signal attenuation) and increases the susceptibility to structural defects from growth or fabrication causing open-circuit failures. (2) Scaling down the graphene electrode dimensions drastically increases the impedance due to quantum capacitance[43], an intrinsic property of graphene due to its unique band structure[44].

In this work, we overcome these challenges and demonstrate completely transparent, high-density, high-channel-count (up to 256 channels) microelectrode arrays with ultrasmall graphene electrodes for multimodal experiments. We reduced the sheet resistance of graphene wires sevenfold by adopting double-layer graphene (DLG) and interlayer nitric acid (HNO_3) doping and realized high-aspect-ratio graphene wires with high yield. To overcome the quantum capacitance and lower the impedance of small graphene electrodes, we employed platinum nanoparticles (PtNPs) and achieved low impedances (~250 kΩ) for electrodes with 20 μm diameter. Overall, our high-density graphene electrodes provide the smallest electrode size, highest channel count and density, largest coverage, highest optical transmittance and lowest normalized impedance among all other transparent neural interfaces (Extended Data Table 1, Extended Data Fig. 1 and Supplementary Discussion 1). We implanted these arrays over the visual cortex of mice and performed simultaneous two-photon calcium imaging at different depths, namely, 50 and 225 μm, corresponding to layer 1 (L1) and layer 2/3 (L2/3), respectively. The small size of graphene electrodes and their large coverage enabled us to detect low- and high-frequency activities on the cortical surface with a high spatiotemporal resolution and examine their correlation with calcium activity at depth. Leveraging the high correlation between calcium activity and surface potentials, we employed dimensionality reduction methods and recurrent neural networks to infer the calcium activity at depth from the surface potentials at population and cellular levels.

Results

Defect-free low-resistance transparent graphene wires

Complete transparency of the graphene array is crucial for multimodal experiments with a completely clear FoV. Previous designs of transparent graphene arrays using single-layer graphene (SLG) had gold wires surrounding the recording electrode area, which limited the FoV and increased the risk for light-induced artefacts[14]. The severity of optical blocking or shadows and light-induced artefacts depends on the experimental parameters and the type of optical modality used. To further investigate these effects during two-photon imaging, we conducted characterization experiments using both gold and graphene electrodes (Extended Data Fig. 2a–c and Supplementary Discussion 2). The characterization results revealed that gold wires create shadows that obscure neurons (Extended Data Fig. 2d) and produce

light-induced artefacts, whereas graphene electrodes allow for clear imaging without such interference (Extended Data Fig. 2e,f). Gold electrodes drastically distort the neural signal with the harmonics of the scanning frequency, whereas graphene electrodes provide artefact-free recordings, emphasizing the necessity of using graphene for transparent high-density microelectrode arrays (Supplementary Discussion 2).

To build high-density graphene arrays with an extended fully transparent recording area, we needed to miniaturize the graphene wires without causing a substantial increase in wire resistance. However, unlike conventional metal microwires with finite thicknesses, graphene has a relatively high sheet resistance due to its single-plane two-dimensional atomic structure and grain boundaries. Therefore, reducing the width and increasing the length of graphene wires can drastically increase the wire resistance and may lead to the attenuation of the recorded signals. Furthermore, thin and long graphene wires are susceptible to defects in growth and fabrication processes, which can subsequently lead to open circuits in the graphene wires and reduce the yield of the microelectrode array.

Here we addressed these challenges by introducing interlayer-doped double-layer graphene (id-DLG) to build flexible and transparent arrays with low-resistance long graphene wires and ultrasmall microelectrodes (Fig. 1a,b). Details of the fabrication steps are explained in the Methods section. Our id-DLG approach was effective not only in eliminating the defects formed during the growth or fabrication of graphene (Fig. 1c) but also in reducing the sheet resistance of graphene wires from 1,908 Ω sq^{-1} for SLG to 276 Ω sq^{-1} for id-DLG (Fig. 1d and Supplementary Discussion 3). By addressing the graphene defect (Extended Data Fig. 3) and sheet resistance issues, our id-DLG approach allowed us to realize high-density arrays with an extended transparent FoV for artefact-free multimodal experiments (Fig. 1a,e). We fabricated 64- and 256-channel arrays with 20 μm openings, 350 μm centre-to-centre pitch and total clear areas of 3.1×2.8 mm^2 (Fig. 1a) and 6.4×6.1 mm^2 available for imaging, respectively (Fig. 1e and Supplementary Fig. 1a,b). Moreover, we designed and fabricated different configurations of transparent arrays tailored to meet the specific requirements of distinct in vivo experiments (Supplementary Fig. 1c–e).

Overcoming quantum capacitance for ultrasmall electrodes

Miniaturizing graphene electrodes to single-cell dimensions results in large impedances because of the quantum capacitance of graphene, which is attributed to the low density of states near the Dirac point[43]. Employing multilayer graphene and introducing dopants can increase the quantum capacitance[15,43], but it still dominates the overall capacitance (Fig. 2a and Methods). To reduce the impedance, we electrochemically deposited PtNPs, a method suggested to bypass the limits of the quantum capacitance effect by creating a low-impedance parallel conductance path. PtNP modifies the capacitive electrode/electrolyte interface dominated by the quantum capacitance of graphene through an increase in the effective surface area and by enabling electrochemical reactions via PtNPs (Fig. 2b). The application of PtNP deposition successfully decreased the average impedance from 5.4 MΩ to 250 kΩ (Fig. 2c).

To quantitatively analyse the electrochemical impedance of electrodes, we constructed an equivalent circuit model (Methods) for id-DLG with and without PtNPs (Fig. 2d). The

measured electrochemical impedance spectroscopy (EIS) data and the fitted equivalent circuit model results are shown in Fig. 2e, and the extracted parameters are listed in Extended Data Table 2 for the PtNP/id-DLG and id-DLG models (Extended Data Fig. 4a and Methods). We observed that the impedance of electrodes decreased and the particle size increased with an increased deposition time (Extended Data Fig. 4b,c). Although the transparency of electrodes covered with PtNPs is reduced, they cover only 0.23% of the total area of the array; therefore, the PtNP/id-DLG arrays maintain high transparency (Fig. 2f). Cyclic voltammetry results before and after 150 s of PtNP deposition indicate that the electrolyte/id-DLG interface is fully capacitive, PtNPs are actively contributing to the charge-transfer process at the electrode/electrolyte interface[43,45] and there is a 7.5-fold increase in the charge storage capacity following PtNP deposition (Extended Data Fig. 4d and Supplementary Discussion 4). Moreover, our results show that the length and resistance of the graphene wires have a negligible effect on the electrode characterization results and electrophysiological recordings (Extended Data Fig. 4e and Supplementary Discussion 5). Overall, these results demonstrate the successful integration of id-DLG and PtNP to realize high-yield fully transparent graphene arrays with ultrasmall electrodes and low impedance for multimodal experiments with uncompromised signal quality.

In vivo multimodal experiments with transgenic mice

We performed multimodal experiments with transparent PtNP/id-DLG arrays to record electrophysiological signals from the cortical surface while conducting calcium imaging with two-photon microscopy from the ipsilateral visual cortex of transgenic mice expressing GCaMP6s in most cortical excitatory neurons (Methods and Supplementary Discussion 6). We performed simultaneous electrophysiology recording and calcium imaging at two different depths (L1 and L2/3) as the animals were presented with drifting gratings as a visual stimulus (Fig. 3a and Methods). The high optical transparency of the implanted array allowed for the easy detection of excitatory neurons and their compartments and recording calcium signals with a single-cell resolution (Fig. 3b). Representative electrical signals recorded from the 64 graphene electrodes are demonstrated in Fig. 3c. Trial-averaged calcium activity of L2/3 excitatory neurons (Fig. 3d and Methods) and representative optical signals from L1 and L2/3 (Fig. 3e–g) highlight the diverse range of neuronal responses elicited by drifting gratings (Supplementary Discussion 6). To ensure that the electrophysiology recordings were consistent over the cortex, we examined the noise level of recorded signals and showed that it is uniform across the array, regardless of the wire lengths (Extended Data Fig. 5a,b and Methods). The imaging quality was also not compromised by the transparent graphene array and the ultrasmall PtNP electrodes did not obstruct the FoV (Extended Data Fig. 5c,d).

Our flexible array enabled us to record the surface potentials from 64 channels that spanned over a large area (2.5×2.5 mm^2) of the cortex (Fig. 4a). With such a broad spatial coverage, we were able to examine the propagation of visual stimulation responses (Fig. 4b). We analysed the power of visually evoked responses at different frequency bands and found that the high-frequency bands (γ and MUA) were more localized compared with the low-frequency bands (δ and θ), which propagated to the other cortical areas (Fig. 4c and Methods), consistent with previous works[33,46,47]. The small electrodes (20

μm) with low impedances allowed us to record the MUA from the cortical surface with high fidelity. Figure 4d illustrates the representative event-triggered MUA waveforms for select channels, distinguished by different colours, indicating that the detected MUA events are fairly localized over the cortex. These short-duration spikes recorded from the surface were classified as MUA since their autocorrelograms did not show any refractory period (Supplementary Fig. 2a). To investigate the origins of MUA spikes detected on the surface, we examined the correlation between cellular signals from calcium imaging and the MUA power for each channel (Methods). The high correlation between the cellular calcium peaks and the MUA power for the channels within the FoV suggests that the spiking activity of L2/3 excitatory neurons underneath these channels is an important contributor to the MUA detected on the surface (Fig. 4e). Representative cell-averaged calcium signal and MUA power of the channel with the maximum correlation are demonstrated in Fig. 4f and the correlation between calcium peaks and MUA power extracted from the whole recording is shown in Fig. 4g. We found similar correlation values between the MUA power and cell-averaged calcium signal in other experiments (Supplementary Fig. 2b–e).

Predicting neural activity at depth from surface recordings

Given the correlation between the MUA power recorded from the surface and the cellular calcium signals imaged in L2/3, we asked whether it is possible to predict the brain activity at deeper layers by using only high-resolution electrical recordings from the cortical surface. We implemented an artificial neural network model that consists of a linear hidden layer, a single-layer bidirectional long short-term memory (BiLSTM) network, and a linear readout layer (Fig. 5a and Methods)[10,48]. The models were trained using the multimodal datasets to learn the nonlinear relationships between cellular calcium activities and surface potentials (Methods). The calcium activity predicted from the surface potentials shows good agreement with the ground-truth calcium fluorescence change for both layers (Fig. 5b). To evaluate the contributions spatially provided by different channels, we performed the decoding using subsets of channels starting from those closest to the FoV (Supplementary Fig. 2f). The decoding performance increased with the inclusion of more channels (Fig. 5c), which indicates that different channels provide complementary information. However, the decoding performance was saturated when ~20 channels were used, suggesting that additional channels provide redundant information beyond this point. We then investigated the contribution of different frequency bands and found that the best decoding performance is achieved when MUA, γ and H-γ were included, suggesting that the high-frequency components carry a vast amount of information on the neural activity including cellular spiking in the FoV (Fig. 5d and Supplementary Fig. 2g).

Predicting cellular calcium activity from surface recordings

We next investigated a more interesting question, which is whether predicting calcium fluorescence of single cells from deeper layers is possible by only using high-resolution recordings of cortical potentials. Developing a network similar to that shown in Fig. 5a to predict the activity of all the 136 neurons would require increasing the complexity of the network, which is not efficient due to the covariances in neural activity. Previous studies have shown that the neural activity of neurons could be defined by low-dimensional

manifolds that capture most of the variance[49,50]. Therefore, a better approach would be to predict the low-dimensional neural manifolds and project them back to the single-cell space.

To investigate the feasibility of predicting the single-cell activities of L2/3 neurons from the surface potentials, we first used Gaussian process factor analysis (GPFA) to find a low-dimensional latent space that is very representative of the high-dimensional calcium fluorescence signal (Methods and Supplementary Fig. 3a). We trained models to predict each of the latents (Supplementary Fig. 3b) and projected the decoded latent variables to the high-dimensional space to reconstruct the single-cell calcium fluorescence (Extended Data Fig. 6 and Methods). Our decoding model (Fig. 6a) successfully inferred the calcium activity of several neurons at depth using the electrical activities recorded from the cortical surface (Fig. 6b,c). The efficacy of information extraction by the GPFA model is critical for the decoding performance; an optimized representation of population activity provides more comprehensive data, which, in turn, enhances the decoding accuracy (Supplementary Fig. 4a,b). We also found that the decoding performance is significantly better for cells that are responsive to the visual stimulus (Supplementary Fig. 4c and Methods).

Next, we investigated whether the high accuracy of our decoding model can be attributed to the low variance of drifting gratings and the population coupling of neurons in response to the visual stimulus. It has been shown that the spontaneous activity in the visual cortex is complex and potentially higher dimensional than the evoked responses[51], with population couplings that resemble those observed in response to complex visual stimuli such as natural images[52,53]. Therefore, we applied our decoding strategy to a separate dataset acquired from sessions without any visual stimulus (Methods). We successfully inferred the calcium activity of single neurons in spontaneous sessions (Extended Data Fig. 7). To investigate the effect of population coupling on single-cell calcium activity inference, we computed the population couplings for both evoked and spontaneous sessions (Extended Data Fig. 8a,b and Supplementary Discussion 7). By exploring the relationship between the population coupling and single-cell decoding results, we showed that a higher coupling does not always imply better decoding performance. For instance, in both evoked and spontaneous sessions, we found highly coupled cells with poor decoding performance and top decoded cells with low population couplings (Extended Data Fig. 8c,d). Therefore, we focused on the top decoded cells and by examining their population couplings, we discovered that the decoding accuracy of the top inferred cells was consistently better in the evoked sessions, despite having a lower population coupling compared with the spontaneous sessions (Extended Data Fig. 8e–h). These findings suggest that although population coupling might potentially contribute to the inference of calcium activity of individual cells, it cannot be the sole contributing factor that determines the decoding performance.

Overall, the decoding results for evoked and spontaneous sessions indicate that the surface potentials recorded by transparent PtNP/id-DLG arrays carry information about the neuronal activities in both superficial and deep layers of the brain and could be used to infer neural population dynamics even at the single-cell level.

Conclusions

In this work, we developed a transparent, high-density graphene array with ultrasmall electrodes and demonstrated its application in multimodal experiments to study the neural dynamics at different cortical layers with complementary spatiotemporal resolution provided by optical imaging and electrophysiological recording. Complete transparency of the graphene arrays enabled us to perform artefact-free multimodal experiments combining electrical recordings from the surface with two-photon imaging at depth. We used the multimodal datasets and trained artificial neural networks to infer the calcium activity at different layers of the visual cortex. We successfully demonstrated the inference of calcium activity at both average and cellular resolutions using the surface potentials. Though our cellular decoding model may not capture the calcium activity for all the cells in the FoV, this limitation presents an opportunity for future improvement through optimizing the dimensionality reduction methods and decoding models as well as constructing more comprehensive training datasets. Moreover, the dimensionality reduction step can be further improved to enable the joint latent modelling of electrical and optical recordings. Proper extraction and understanding of shared embeddings in these modalities is needed to allow for the generalization of our methodology to experiments with only one modality, such as electrophysiological recordings with no simultaneous optical imaging. Generalization of the models could enable the imaging of neural activity across the cortex in freely moving animals, without the requirement for head-fixed microscopy configurations that constrain the animal's behaviour. The head-fixed configuration, along with issues related to the photobleaching of indicators, impose a strict limit on the total duration of imaging experiments, typically not exceeding a couple of hours. In contrast, electrophysiological recordings do not suffer from such limitations and can be continuously performed in freely moving animals over extended periods of time. Our multimodal approach can be seamlessly applied to extend the time frame for continuous imaging experiments, ranging from just a few hours a day[54] to potentially spanning days, weeks or even months.

Our results demonstrate that transparent graphene arrays could be potentially integrated with other techniques to facilitate multimodal experiments with unprecedented spatiotemporal resolutions. The recordings of neural activity at depth through generalized cross-modality inference models without using invasive neural implants have the potential to improve the longevity of brain–computer interface technologies, which could pave the way for medical translation. This approach can also enhance the interpretation of electrophysiology studies by reducing the damage to brain tissue, which is a limitation in studies with laminar probes[55–57]. These multimodal experiments could expand the spatial reach of neural recordings and facilitate the source localization of distinct features, thus having implications for enhancing the capabilities of existing brain–computer interface technologies in tackling complex motor and behavioural tasks. Ultimately, a generalized model with the capability of predicting neural activity at depth from surface recordings has the potential to open up new possibilities for developing minimally invasive neural prosthetics or targeted treatments for various neurological disorders.

Online content

Any methods, additional references, Nature Portfolio reporting summaries, source data, extended data, supplementary information, acknowledgements, peer review information; details of author contributions and competing interests; and statements of data and code availability are available at https://doi.org/10.1038/s41565-023-01576-z.

Methods

Fabrication of high-density transparent graphene arrays

To form the transparent and flexible substrate, we deposited a 14-µm-thick layer of parylene C (PC) on a four-inch silicon wafer coated with 100 nm PMGI SF3 as the sacrificial layer. Next, we sputtered 5 nm chromium and 100 nm gold on the PC substrate and patterned it with photolithography and wet etching to form metal wires and contact pads. The first graphene layer was transferred using an electrochemical delamination process[14,58]. To decrease the wire resistance, it was immersed into 50% HNO_3 solution for 10 min. After cleaning the HNO_3-doped graphene with acetone and isopropyl alcohol, the second graphene layer was transferred using the same process as the first layer. To pattern the DLG, we used a bilayer photoresist (PMGI/AZ1512) and etched the graphene with oxygen plasma, followed by acetone/isopropyl alcohol cleaning. To protect the DLG during the next steps, we sputtered a 25 nm silicon dioxide etch-stop layer on the patterned graphene. Then, we deposited PC (2 µm) as the encapsulation layer and patterned it with oxygen plasma to define the electrode openings. To remove the protective silicon dioxide layer and get access to the DLG, we used a 6:1 buffered oxide etchant. Finally, we detached the arrays from the wafer by immersing it in acetone and applying slight physical force to the edges of the wafer.

PtNP deposition and electrode characterization

The electrochemical deposition of PtNPs and electrochemical characterizations were conducted with Gamry 600 plus and 1× phosphate-buffered saline. Both EIS and cyclic voltammetry were measured under a three-electrode configuration using Ag/AgCl as the reference electrode and platinum as the counter electrode. To avoid electromagnetic noise, all the measurements were conducted inside a Faraday cage. PtNP deposition was conducted under a two-electrode configuration in a H_2PtCl_6 (0.05 M) and K_2HPO_4 (0.01 M) solution, with a 50 nA current flown from the id-DLG electrode to the counter electrode under ambient conditions. Since the impedance of the electrodes saturated after 150 s of PtNP deposition (with a value of around 200 kΩ), we decided to set the deposition time to 150 s.

Equivalent circuit models

To quantitatively analyse the electrodes, we modified the conventional Randles model to capture the quantum capacitance effect, resistance of graphene wires and pseudo-capacitance of PtNP. Unlike a previously reported circuit model for the PtNP/SLG electrode[43], there is no need for a parallel branch to explain the electrochemical reaction at the electrolyte/electrode interface as the graphene electrode openings are completely covered by PtNPs and the interface is converted from electrolyte/id-DLG to electrolyte/

PtNP. Therefore, the quantum capacitance component is removed from the equivalent circuit model for the electrode/electrolyte interface and C_p and R_{ct} are added to represent the pseudo-capacitance of PtNP.

To extract the capacitances in the equivalent circuit models, we first obtained the values of CPE_{Gr} and C_Q by fitting the EIS measurement data to the circuit model of the id-DLG electrode. Then, we extracted the CPE parameters (capacitance parameter Y and phase-change element exponent α) and used equation (1) to calculate the C_{dl} value[59]. Here R_s is the solution resistance.

$$C_{dl} = \frac{(Y \times R_s)^{\frac{1}{\alpha}}}{R_s}$$

(1)

We used equation (2) and the measured open-circuit voltage to calculate the impurity concentrations for SLG, DLG and id-DLG[43,44].

$$C_Q = \frac{2e^2}{\hbar v_F \sqrt{\pi}} \left\{ \left(\frac{eV}{\hbar v_F \sqrt{\pi}} \right)^2 + |n*| \right\}^{1/2}$$

(2)

Here v_F is the Fermi velocity, $\hbar$ is the Planck constant and V is the open-circuit voltage. To plot the capacitances shown in Fig. 2a, we used equation (2) and swept the open-circuit voltage from −0.4 to 0.4 V (C_{dl} is not a function of V, so its value is constant).

Animal procedures

All the procedures were performed in accordance with the protocols approved by the University of California San Diego's Institutional Animal Care and Use Committee and guidelines of the National Institute of Health. Three animals were used in this study. Adult mice (cross between CaMKIIa-tTA (JAX 003010)[60] and tetO-GCaMP6s (JAX 024742)[61], two months old) were anaesthetized with isoflurane (3% for induction and 1% for maintenance). Both eyes were protected by Vaseline, and a circular piece of scalp was removed. After cleaning the underlying bone using a razor blade, a custom-built head plate was implanted to the exposed skull (~1 mm posterior to the lambda) with cyanoacrylate glue and cemented with a dental acrylic (Lang Dental). Two stainless steel screws (F000CE156, J.I. Morris) were implanted over the olfactory bulb as the reference and ground. A square craniotomy was made over the left hemisphere (~3.50 × 4.00 mm, centred at ~1.75 mm lateral and 2.00 mm posterior to the bregma), and the dura of the craniotomized area was carefully removed with a hooked needle. The transparent PtNPs/id-DLG electrode array was first attached to a glass window with ultraviolet glue and connected to the amplifier board. Then, the assembled interface was gently placed onto the exposed cortex with the electrode array facing the cortical surface. The glass window was gradually pressed down through a

micromanipulator (Sutter Instrument) until the whole electrode array was tightly attached to the cortical surface. Although our target area of the brain was the primary visual cortex (V1), other neighbouring cortical areas were covered by the array including the primary somatosensory cortex (S1), posterior parietal cortex (PPC) and retrosplenial cortex (RSC). Vetbond (3M) was applied to fill the gap between the skull and the glass window, and the glass window was further secured with cyanoacrylate glue and dental acrylic. A cocktail of dexamethasone (2.0 mg kg^{-1} body weight), buprenorphine (0.1 mg kg^{-1} body weight) and Baytril (10.0 mg kg^{-1} body weight) was given at the end of the surgery. The animal was fully recovered from anaesthesia before recording.

Visual stimulation

Square-wave drifting grating stimuli (100% contrast, 0.04 cycles per degree, 3 cycles per second, covering the entire contralateral receptive field) were presented on an LCD monitor (30×38 cm^2) positioned 15 cm away from the right eye using Psychtoolbox (http://psychtoolbox.org/). Each of the eight orientations (45° apart) were presented for 2.0 or 2.5 s on each trial in a pseudorandom order, with an 8 s interstimulus interval. We presented each orientation at least 30 times in a session. Moreover, we conducted experiments to record the spontaneous activities without any stimuli.

Two-photon imaging and analysis of imaging data

Two-photon imaging was conducted for a head-fixed awake mouse through a ×16, 0.8-numerical-aperture objective (Nikon) mounted on a commercial two-photon microscope (B-Scope, Thorlabs) and using a 925 nm laser (Ti:sapphire laser, Newport). The images were acquired at ~29 Hz and a resolution of 512×512 pixels, covering 960×960 μm of the V1 area (Fig. 3b). The laser power was ~15 mW for imaging L1 (~50 μm deep) and ~40 mW for imaging L2/3 (~225 μm deep). The acquired images were motion corrected offline[62]. For the quantification of calcium signals from L1, pixels in the blood vessels and ten pixels close to the frame edges were excluded. The fluorescence time course (F) was calculated as the ground average of the remaining pixels in each frame. At each time point, the baseline (F_0) was estimated by the tenth percentile of the fluorescence distribution. For the quantification of calcium signals from L2/3 cell bodies, regions of interest (ROIs) were first identified by the Suite2p package[63] and then visually inspected to remove the non-somatic ones. Next, the fluorescence time course of each cellular ROI and its surrounding neuropil ROI was extracted using the Suite2p package. Then, the fluorescence signal of a cell body was estimated as $F_{cellbody} = F_{cellRoI} - 0.7 \times F_{neuropilRoI}$. Finally, $\Delta F/F_0$ was computed as $(F_{cellbody} - F_0)/F_0$, where F_0 is the eighth percentile of the intensity distribution during the recording session. Unlike L2/3, L1 is mainly occupied by intermingled neuropils, including dendrites and axons extended from deeper layers and its fluorescence represents dendritic and axonal activities. Therefore, for L1, we used the average (pixel-level) fluorescence changes in the FoV, excluding the blood vessels.

To analyse the stimulus response of the imaged cells in L2/3, we subtracted the baseline activity (2 s before the stimulus onset) from the trial-averaged fluorescence signal for each cell body and normalized it with the baseline activity. To categorize the cells, we sorted them based on their averaged normalized stimulus response from 0.3 to 3.0 s after the

stimulus onset. We considered the first and last 20 cells as modulated and rest of the cells as non-modulated cells.

Electrophysiological recordings and noise characterization

Electrophysiological recordings were conducted with the RHD2000 amplifier board and RHD2000 evaluation system (Intan Technologies). The sampling rate was set to 20 kHz, and the d.c. offset was removed with the recording system's built-in filtering above 0.1 Hz. The Intan data were imported into MATLAB (MathWorks) and analysed using custom scripts in MATLAB v. 2022b. To characterize the noise level, we calculated the standard deviation of the bandpass-filtered (0.5–4.0 kHz) signals for all the channels and plotted it as a function of wire length for all the electrodes (Extended Data Fig. 5a,b).

Electrophysiology data analysis and correlation with calcium activity

Electrodes with impedances above 10 MΩ were excluded from the analyses. To remove common artefacts (imaging and power line), a bank of notch filters was applied to the surface recordings (the filters were separately optimized for each channel). The signals were lowpass filtered below 250 Hz using a fourth-order Butterworth filter to extract the local field potentials. The visually evoked potentials for each trial were extracted from the local field potentials and the trial-averaged peak-to-peak amplitude and propagation delay of the stimulus responses were visualized using two-dimensional colour maps. To further filter the signals into common low-frequency bands (δ, 1–4 Hz; θ, 4–7 Hz; α, 8–15 Hz; β, 15–30 Hz; γ, 31–59 Hz; H-γ, 61–200 Hz), sixth-order Butterworth bandpass filters were applied with the corresponding frequency ranges. The MUA was extracted by applying a sixth-order bandpass filter from 0.5 to 4.0 kHz followed by common average referencing. The powers at different bands (δ, θ, α, β, γ, H-γ and MUA) were calculated by taking the square of the bandpass-filtered signals and applying a 100 ms Gaussian filter to reduce the noise. The power changes due to visual stimulus were calculated by trial averaging the powers at different bands and subtracting the baseline activity (2 s before stimulus onset) and the peak of the power changes (in a 4 s window after the stimulus onset) were demonstrated using two-dimensional spatial maps to visualize the localization of different bands. To detect the MUA events, we applied the threshold-crossing method on bandpass-filtered (0.5–4.0 kHz) signals with a threshold set at −4 times the standard deviation. To compute the event-triggered MUA averages, we identified the MUA event times for a target channel and calculated the average MUA waveform for all the 64 channels, spanning a time window of 1 ms before to 1 ms after each event in the target channel.

To analyse the MUA and average cellular calcium correlation, we first determined the peaks of the normalized cell-averaged $\Delta F/F$ ('findpeaks'; the minimum peak height is set to 0.75) and then took the time average of the MUA power in a 2 s window [−1.5 s, 0.5 s] around the onset times of those peaks for all the 64 channels. The Pearson correlation values were calculated for each channel between the calcium peaks and the averaged MUA powers. The same procedure is followed to calculate the correlation of the average cellular calcium activity with other frequency bands (δ, θ, α, β, γ and H-γ).

Decoding model for prediction of calcium activity

Python (version 3.6.9) was used to develop the inference models. A neural network model with a sequential stack of a linear hidden layer, one BiLSTM layer and a linear readout layer was implemented. Batch normalization and dropout ($p = 0.3$) were used for improved training and a rectified linear unit as the activation function. The surface potential power at different frequency bands (δ to MUA) were downsampled to match the sampling rates of the calcium signal (29 Hz) and clipped with a threshold of 95 percentile to suppress the potential artefacts. These signals were then used as inputs to the neural network model. To decode the neural activity at time step t, the power segments within $[t - 1.5 \text{ s}, t + 1.5 \text{ s}]$ were used (total time steps, 90). The first linear layer had 25 neurons and the BiLSTM had 15 hidden neurons. The last layer outputs the predicted cell-averaged calcium signal.

Adam was used to train and optimize the parameters of the model, with the following parameters: learning rate = 6×10^{-5}, beta1 = 0.9, beta2 = 0.999, epsilon = 10^{-8}. The batch size was set to 128 and the training converged within ~20 epochs. The mean squared error was used as the loss function. Fivefold cross-validation was performed by splitting the 40 min recordings into 8 min segments. The Pearson correlation between the decoded and ground-truth data was used to evaluate the model performance. The correlation values were averaged over five folds to get a single value for the decoding performance.

Low-dimensional latent space of population activity

We used GPFA—a generative model that unifies dimensionality reduction and smoothing in one framework—for the extraction of latent representations that describe the shared variability of high-dimensional data[64]. We identified eight distinct latent variables that explain most of the variance of the high-dimensional data (Supplementary Fig. 3a). GPFA models observations as a Gaussian model that is related to the latent variable through the following equation:

$$y_{:,t} \mid x_{:,t} \approx N(Cx_{:,t} + d, R)$$

(3)

Here $x_{:,t}$ represents the latent variable at time point t, d is the signal mean, C is the factor loading matrix and R represents the covariance matrix. The ith latent variable x is modelled as a Gaussian process with a covariance matrix K that correlates the latent variables across time points:
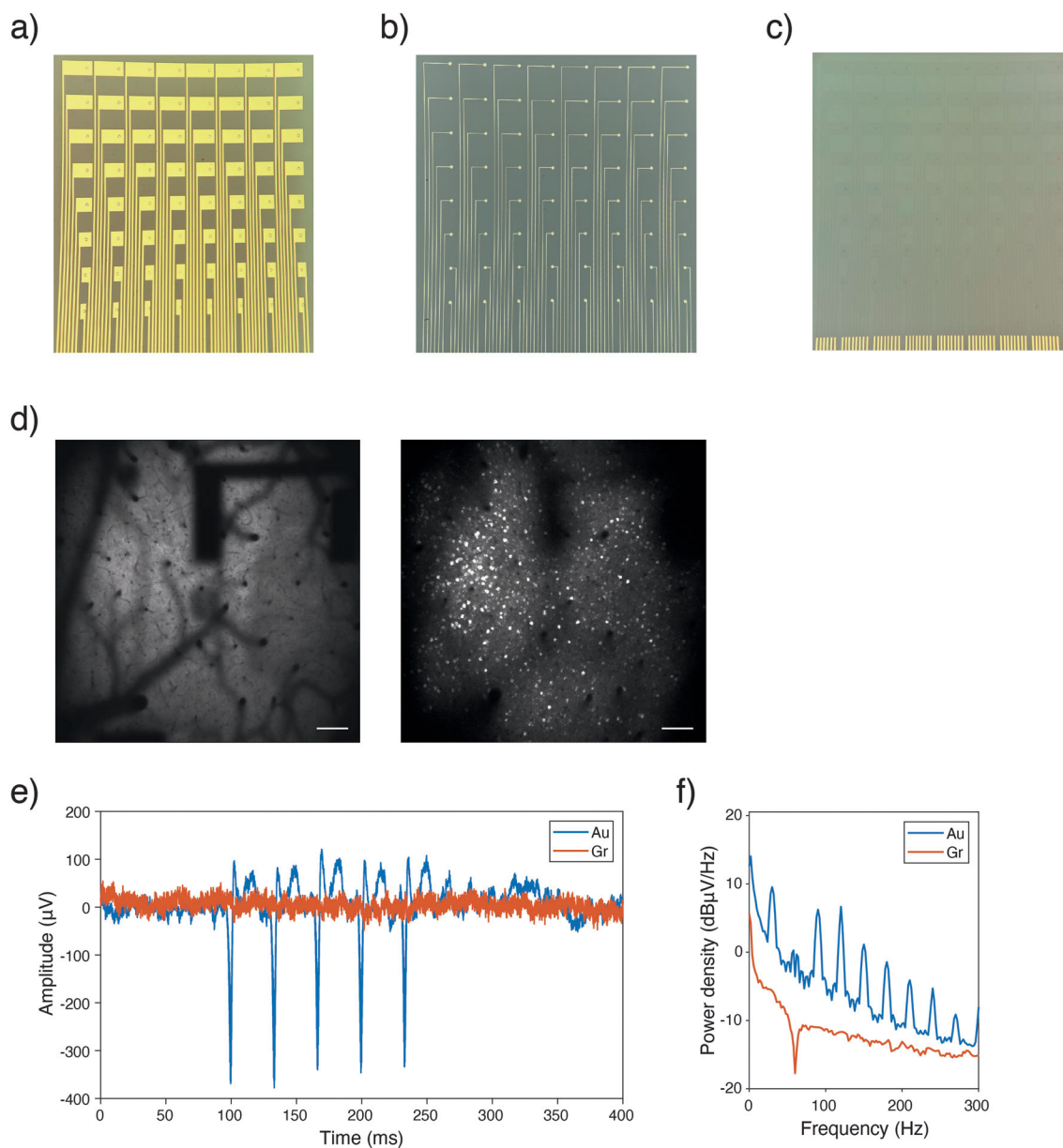
$$x_i \approx N(0, K_i).$$

(4)

Using the training data of calcium signal Y, we train a GPFA model that learns the parameters and infers the trajectory of latent variable x.

$$E[X \mid Y] = KC'(CKC + R)^{-1}(Y - d)$$

(5)

We used the latent variable x and the inferred latent variable $\hat{x}$ from the BiLSTM model to project into a single-cell calcium activity space (Extended Data Fig. 6).

$$E[\widehat{Y}] = CX + d$$

(6)

$$E\left[\widehat{\widehat{Y}}\right] = C\widehat{X} + d$$

(7)

Here $\widehat{Y}$ is the projected calcium signal using the originally inferred latent variables and $\widehat{\widehat{Y}}$ is the projected calcium signal using the latent variables predicted by the BiLSTM model. The projected calcium signals are then compared with the true calcium signals.

Statistics and reproducibility

Two-sided Wilcoxon rank sum test was used to compare the decoding performances of the modulated ($n = 40$) and non-modulated ($n = 96$) cells ($p < 0.001$).

Extended Data

Extended Data Fig. 1 |. Comparison of optical transmittance and normalized impedance of our transparent graphene array with other neural interfaces.
Optical transmittance as a function of normalized impedance for all the electrode technologies listed in Extended Data Table 1.

Extended Data Fig. 2 |. Comparison of conventional gold electrodes with transparent graphene arrays.

(**a**) Conventional 64-channels gold array with 20 μm and (**b**) 6 μm wire widths and smaller gold pads. (**c**) Fully transparent 64-channels graphene array without surrounding gold wires. (**d**) Shadows created by opaque gold wires in the field of view during two-photon imaging at 50 μm (left) and 250 μm (right) depth under the electrodes. The scale bars are 100 μm. (**e**) Signals recorded by gold and graphene arrays shown in b and c during two-photon imaging (at 50 μm depth underneath the electrodes) showing light-induced artifacts in gold but not graphene electrode. (**f**) Power spectral density of signals recorded by gold and graphene electrodes during two-photon Z-scan from 50 μm to 150 μm underneath the electrodes.
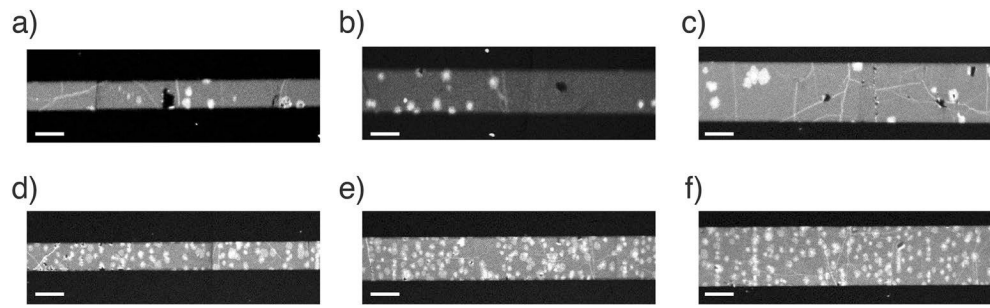
**Extended Data Fig. 3 |. Characterization of defects in SLG and DLG wires.**
(**a**) SLG and DLG wire pinhole images using two-photon microscopy. SLG wire with different width 20 μm, (**b**) 30 μm, and (**c**) 40 μm. DLG wire with different width (**d**) 20 μm, (**e**) 30 μm, and (**f**) 40 μm. Scale bars are 20 μm.
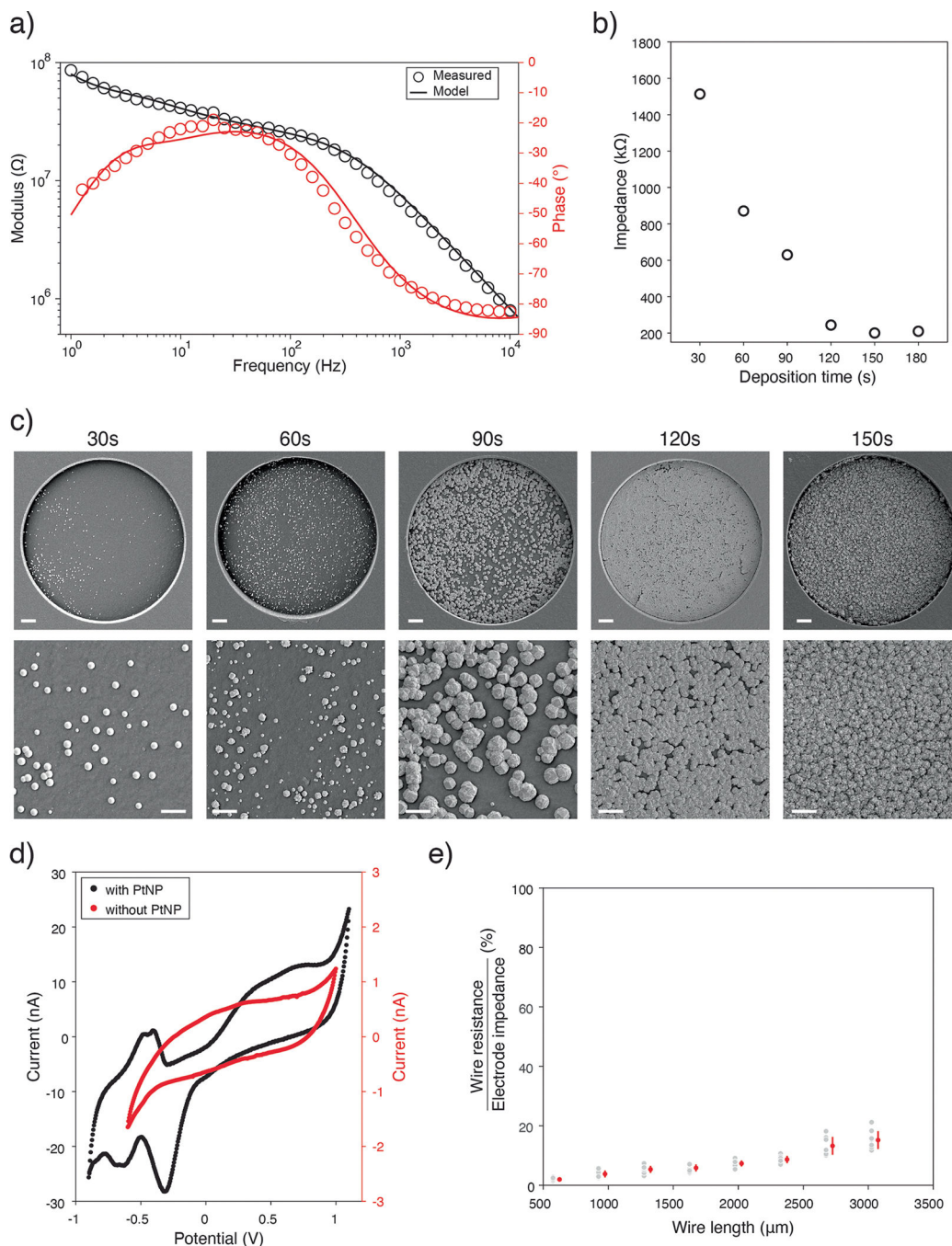
Extended Data Fig. 4 |. Reducing the impedance of electrodes using PtNP deposition.
(**a**) Measured electrochemical impedance spectroscopy (EIS) and the fitted values using
the equivalent circuit model for id-DLG electrode. (**b**) The Impedance of PtNP/id-DLG
with various PtNP deposition time measured at 1 kHz. (**c**) SEM images of PtNP/id-DLG
with various PtNP deposition times. Scale bars are 3 μm and 1 μm in the top and bottom
row, respectively. (**d**) Cyclic voltammetry (CV) measurement result for id-DLG (red) and
PtNP/id-DLG (black). (**e**) The ratio of the graphene wire resistance (R_{Gr}) to the electrode
impedance ($Z_{Electrode}$ - R_{Gr}) for channels with different wire lengths. The gray dots in the

graph represent the ratios for individual channels, while the red dots and bars indicate the mean and standard deviation, respectively, for groups of eight channels (n = 8) with similar wire lengths.
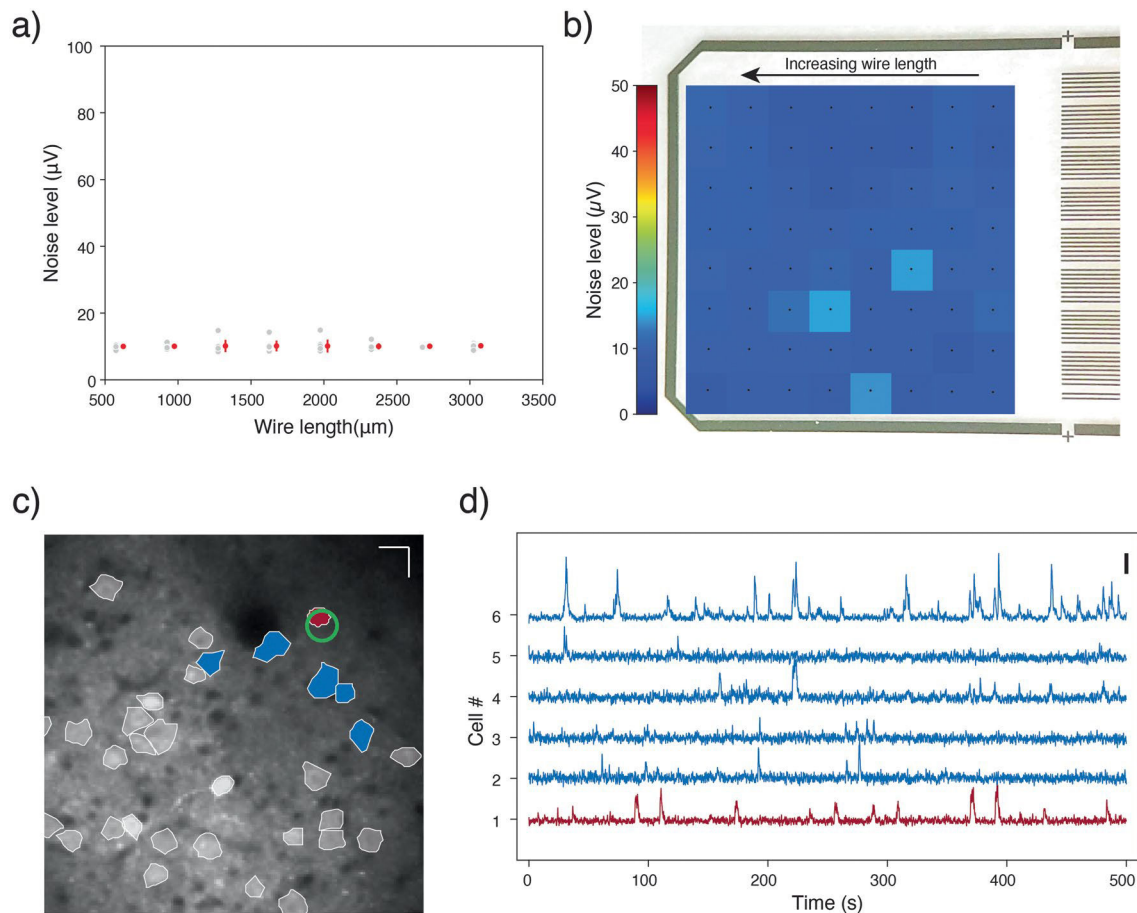

Extended Data Fig. 5 |. Transparent graphene arrays do not affect the signal quality.
(**a**) The noise level of all channels with different graphene wire lengths. The gray dots in the graph represent the noise level for individual channels, while the red dots and lines represent the mean and standard deviation of each group of eight channels with same graphene wire length. (**b**) The heatmap of noise level of all channels overlaid with microscope image of the 64-channel array. (**c**) Pyramidal cells around (blue ROIs) and underneath (red ROI) the electrode (green circle) and (**d**) their F/F signals show that the PtNP/id-DLG electrode does not obstruct the FoV and affect the two-photon signal quality. Scale bars in c and d indicate 20 μm and 5 z-score, respectively.
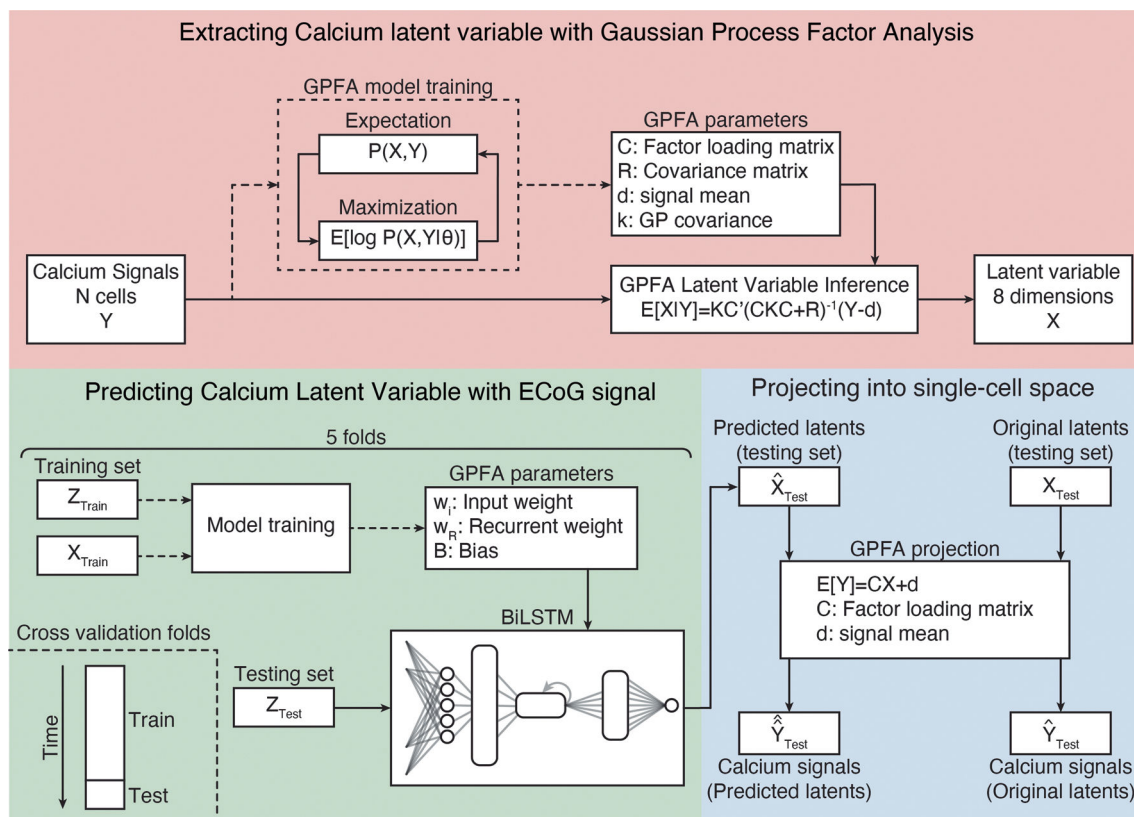
Extended Data Fig. 6 |. Schematic of the decoding model used for single-cell calcium inference. The main steps of the single-cell calcium inference pipeline are explained in detail. Calcium latent variables are extracted using GPFA (red panel) and predicted by the ECoG powers at different frequency bands (green panel). The predicted calcium latents are then projecting into single-cell space (blue panel).
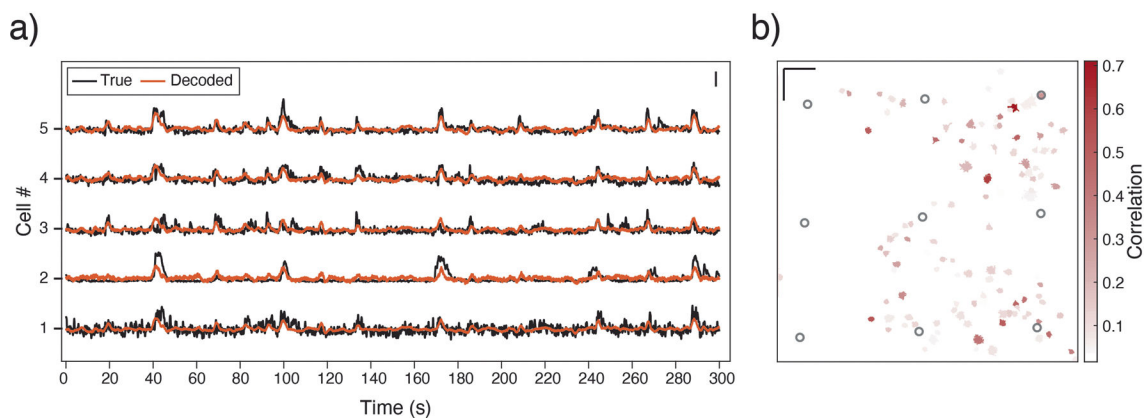
Extended Data Fig. 7 |. Decoding spontaneous calcium activity at single-cell resolution. (**a**) Representative examples for decoded (orange) vs ground truth (black)   F/F of five best-decoded cells in the spontaneous session. The scale bar is 3 z-score. (**b**) Decoding results for all 114 cells in the spontaneous session presented with their locations outlined in

the FoV. The 9 channels inside the FoV are marked with black circles. The scale bars are 100 μm.
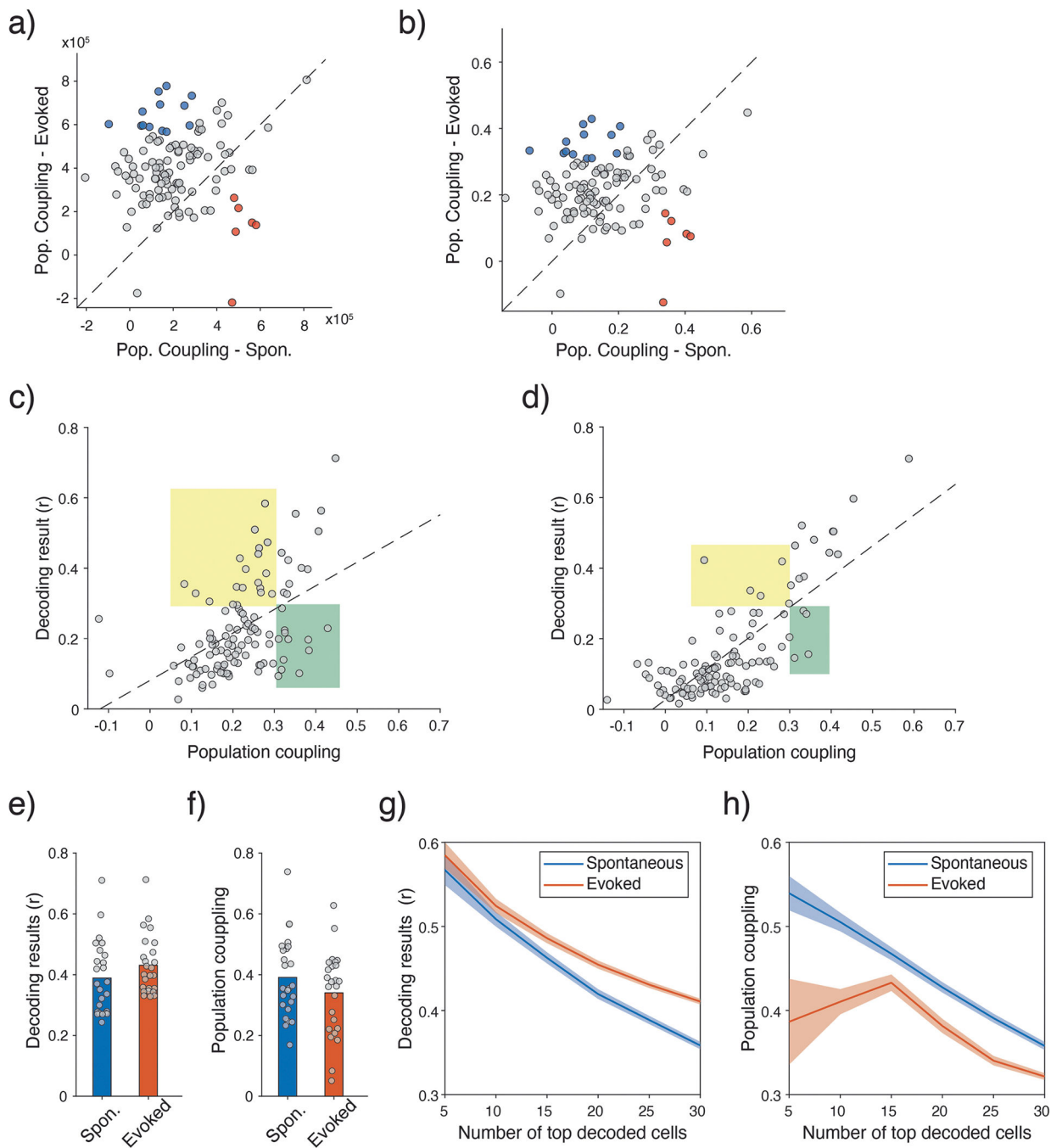
Extended Data Fig. 8 |. The relationship between population coupling and single-cell calcium decoding.

(**a**) Comparison of population coupling across cells (n = 114) in the spontaneous and evoked sessions using method 1 (Eq. 1 in the Supplementary Information), and (**b**) method 2 (Eq. 2 in the Supplementary Information). The red (blue) circles indicate highly coupled cells in the spontaneous (evoked) session with low population coupling in the evoked (spontaneous)

session. (**c**) Decoding results as a function of population coupling for the spontaneous and (**d**) evoked sessions using method 2 (Eq. 2 in the Supplementary Information). The green boxes highlight highly coupled cells with poor decoding results. Yellow boxes highlight cells with high decoding performance, but low population couplings. (**e**) Decoding results and (**f**) population couplings of the top 25 decoded cells in the evoked and spontaneous sessions. (**g**) Decoding results and (**h**) population couplings of the top N decoded cells (N = 5 to 30) in the evoked and spontaneous sessions. Solid lines and shaded regions indicate the mean and s.e.m., respectively. Population couplings are calculated among the top N decoded cells.

Extended Data Table 1 |

Transparent neural recording arrays compatible with multimodal experiments

Material	Electrode area (μm^2)	Channel count	Pitch (μm)	Normalized Impedance ($\Omega^* cm^2$)	Coverage (mm^2)	Transmittance (%)	Chronic Recording	Issues	Reference
	314	**64 (256)**	**350**	**0.78**	**6 (31.3)**	**90**	**Acute**	N/A	**This work**
Gr	2,500	8	300	13.5	0.8	90	Acute	N/A	[12]
	31,400	16	750	76.3	3.6	90	2+ months		[13]
	7,800	16	500	22.3	2.25	90	Acute		[16]
	10,000	16	400	11	1.44	80	Acute		[43]
	10,000	16	500	96.3	2.25	85	Acute		[14]
	10,000	16	500	87.2	2.25	90	20+ days		[48]
	2,500	16	500	22.7	2.25	90	Acute		[15]
	10,000	16	500	140	2.25	85	2+ months		[40]
	10,000	16	500	110	2.25	85	20 days		[38]
ITO	196,350	49	800	21.6	23	90	Acute	Brittle	[17]
	31,400	16	700	6.3	4.4	80	Acute		[18]
	49,090	16	500	14.7	2.25	80	Acute		[20]
CNT	10,000	16	400	20	1.44	85	Acute	Cytotoxicity	[21]
Au	2,500	36	1000	2.57	25	Not reported	14 days	Light-induced artifacts	[21] *
	5,000	32	400	0.6	4	70	20 days		[28]
	31,400	16	700	3.7	4.4	75	Acute		[26]
Ag	53,090	16	850	1.16	1.65	70	2 months		[24]
	102,400	9	2,500	1.22	25	57	Ex-vivo		[22]
	196,000	4	1,000	39.2	1.5	62	Acute		[23]
PEDOT:PSS	706	9	150	1.17	0.09	84	Acute	Delamination	[31]
	490	16	200	0.81	9	85	Acute		[30]
	90,000	16	700	54	4.4	85	Acute		[29]

*
In the Supplementary Information

A comparison of electrode area, channel count, electrode pitch, normalized impedance, areal coverage, optical transmittance, and chronic recording reliability between the state-of-the-art in transparent array technologies and our ultra-high density transparent graphene array.

Extended Data Table 2 |

Parameters in the equivalent circuit models of id-DLG and PtNP/id-DLG

	R_s (kΩ)	R_{Gr} (kΩ)	C_Q ($\mu F/cm^2$)	C_p ($\mu F/cm^2$)	R_{ct} (MΩ)	Y (S.sec^a)	a	W (S.sec$^{1/2}$)	B (sec$^{1/2}$)
id-DLG	25	8.97	9.39	-	20.7	4.35×10^{-11}	9.89×10^{-1}	5.2×10^{-9}	0.51
PtNP/id-DLG	25	8.97	-	80	5.6	3.03×10^{-9}	8.25×10^{-1}	19.0×10^{-9}	1.20

The parameters obtained by fitting the EIS measurements to the equivalent circuit models of the id-DLG and PtNP/id-DLG electrodes.

Supplementary Material

Refer to Web version on PubMed Central for supplementary material.

Acknowledgements

Data availability

The data that support the findings of this study are available within the paper and its Supplementary Information. Other relevant data are available from the corresponding author upon request. Source data are provided with this paper.

References

1. Frank JA, Antonini M-J & Anikeeva P Next-generation interfaces for studying neural function. Nat. Biotechnol. 37, 1013–1023 (2019). [PubMed: 31406326]

2. Machado TA, Kauvar IV & Deisseroth K Multiregion neuronal activity: the forest and the trees. Nat. Rev. Neurosci. 23, 683–704 (2022). [PubMed: 36192596]

3. Logothetis NK et al. Hippocampal–cortical interaction during periods of subcortical silence. Nature 491, 547–553 (2012). [PubMed: 23172213]

4. Gradinaru V et al. Optical deconstruction of parkinsonian neural circuitry. Science 324, 354–359 (2009). [PubMed: 19299587]

5. Fernández-Ruiz A et al. Gamma rhythm communication between entorhinal cortex and dentate gyrus neuronal assemblies. Science 372, eabf3119 (2021). [PubMed: 33795429]

6. Bi X-a et al. A novel CERNNE approach for predicting Parkinson's disease-associated genes and brain regions based on multimodal imaging genetics data. Med. Image Anal. 67, 101830 (2021). [PubMed: 33096519]

7. Zhang D et al. Multimodal classification of Alzheimer's disease and mild cognitive impairment. Neuroimage 55, 856–867 (2011). [PubMed: 21236349]

8. Chiarelli AM et al. Deep learning for hybrid EEG-fNIRS brain–computer interface: application to motor imagery classification. J. Neural Eng. 15, 036028 (2018). [PubMed: 29446352]

9. Halme H-L & Parkkonen L Across-subject offline decoding of motor imagery from MEG and EEG. Sci. Rep. 8, 10087 (2018). [PubMed: 29973645]

10. Liu X et al. Decoding of cortex-wide brain activity from local recordings of neural potentials. J. Neural Eng. 18, 066009 (2021).

11. Siegle JH et al. Survey of spiking in the mouse visual system reveals functional hierarchy. Nature 592, 86–92 (2021). [PubMed: 33473216]

12. Kuzum D et al. Transparent and flexible low noise graphene electrodes for simultaneous electrophysiology and neuroimaging. Nat. Commun. 5, 5259 (2014). [PubMed: 25327632]

13. Park D-W et al. Graphene-based carbon-layered electrode array technology for neural imaging and optogenetic applications. Nat. Commun. 5, 5258 (2014). [PubMed: 25327513]

14. Thunemann M et al. Deep 2-photon imaging and artifact-free optogenetics through transparent graphene microelectrode arrays. Nat. Commun. 9, 2035 (2018). [PubMed: 29789548]

15. Driscoll N et al. Multimodal in vivo recording using transparent graphene microelectrodes illuminates spatiotemporal seizure dynamics at the microscale. Commun. Biol. 4, 136 (2021). [PubMed: 33514839]

16. Park D-W et al. Electrical neural stimulation and simultaneous in vivo monitoring with transparent graphene electrode arrays implanted in GCaMP6f mice. ACS Nano 12, 148–157 (2018). [PubMed: 29253337]

17. Ledochowitsch P et al. A transparent μECoG array for simultaneous recording and optogenetic stimulation. In Proc. 2011 Annual International Conference of the IEEE Engineering in Medicine and Biology Society 2937–2940 (IEEE, 2011).

18. Kwon KY et al. Opto-μECoG array: a hybrid neural interface with transparent μECoG electrode array and integrated LEDs for optogenetics. IEEE Trans. Biomed. Circuits Syst. 7, 593–600 (2013). [PubMed: 24144668]

19. Kunori N & Takashima I A transparent epidural electrode array for use in conjunction with optical imaging. J. Neurosci. Methods 251, 130–137 (2015). [PubMed: 26049111]

20. Ledochowitsch P et al. Strategies for optical control and simultaneous electrical readout of extended cortical circuits. J. Neurosci. Methods 256, 220–231 (2015). [PubMed: 26296286]

21. Zhang J et al. Stretchable transparent electrode arrays for simultaneous electrical and optical interrogation of neural circuits in vivo. Nano Lett. 18, 2903–2911 (2018). [PubMed: 29608857]

22. Chen Z et al. Flexible and transparent metal nanowire microelectrode arrays and interconnects for electrophysiology, optogenetics, and optical mapping. Adv. Mater. Technol. 6, 2100225 (2021).

23. Neto JP et al. Transparent and flexible electrocorticography electrode arrays based on silver nanowire networks for neural recordings. ACS Appl. Nano Mater. 4, 5737–5747 (2021).

24. Araki T et al. Long-term implantable, flexible, and transparent neural interface based on Ag/Au core–shell nanowires. Adv. Healthc. Mater. 8, 1900130 (2019).

25. Seo KJ et al. Transparent electrophysiology microelectrodes and interconnects from metal nanomesh. ACS Nano 11, 4365–4372 (2017). [PubMed: 28391679]

26. Seo JW et al. Artifact-free 2D mapping of neural activity in vivo through transparent gold nanonetwork array. Adv. Funct. Mater. 30, 2000896 (2020).

27. Obaid SN et al. Multifunctional flexible biointerfaces for simultaneous colocalized optophysiology and electrophysiology. Adv. Funct. Mater. 30, 1910027 (2020).

28. Qiang Y et al. Transparent arrays of bilayer-nanomesh microelectrodes for simultaneous electrophysiology and two-photon imaging in the brain. Sci. Adv. 4, eaat0626 (2018). [PubMed: 30191176]

29. Cho YU et al. Ultra-low cost, facile fabrication of transparent neural electrode array for electrocorticography with photoelectric artifact-free optogenetics. Adv. Funct. Mater. 32, 2105568 (2022).

30. Yang W et al. A fully transparent, flexible PEDOT:PSS–ITO–Ag–ITO based microelectrode array for ECoG recording. Lab Chip 21, 1096–1108 (2021). [PubMed: 33522526]

31. Kshirsagar P et al. Transparent graphene/PEDOT:PSS microelectrodes for electro- and optophysiology. Adv. Mater. Technol. 4, 1800318 (2019).

32. Viswam V et al. Optimal electrode size for multi-scale extracellular-potential recording from neuronal assemblies. Front. Neurosci. 13, 385 (2019). [PubMed: 31105515]

33. Rogers N et al. Correlation structure in micro-ECoG recordings is described by spatially coherent components. PLoS Comput. Biol. 15, e1006769 (2019). [PubMed: 30742605]

34. Harris KD et al. Improving data quality in neuronal population recordings. Nat. Neurosci. 19, 1165–1174 (2016). [PubMed: 27571195]

35. Akinwande D et al. A review on mechanics and mechanical properties of 2D materials—graphene and beyond. Extrem. Mech. Lett. 13, 42–77 (2017).

36. Kireev D et al. Continuous cuffless monitoring of arterial blood pressure via graphene bioimpedance tattoos. Nat. Nanotechnol. 17, 864–870 (2022). [PubMed: 35725927]

37. Sahni D et al. Biocompatibility of pristine graphene for neuronal interface. J. Neurosurg. Pediatr. 11, 575–583 (2013). [PubMed: 23473006]

38. Liu X et al. E-cannula reveals anatomical diversity in sharp-wave ripples as a driver for the recruitment of distinct hippocampal assemblies. Cell Rep. 41, 111453 (2022). [PubMed: 36198271]

39. Ding D et al. Evaluation of durability of transparent graphene electrodes fabricated on different flexible substrates for chronic in vivo experiments. IEEE Trans. Biomed. Eng. 67, 3203–3210 (2020). [PubMed: 32191878]

40. Wilson MN et al. Multimodal monitoring of human cortical organoids implanted in mice reveal functional connection with visual cortex. Nat. Commun. 13, 7945 (2022). [PubMed: 36572698]

41. Bonaccini Calia A et al. Full-bandwidth electrophysiology of seizures and epileptiform activity enabled by flexible graphene microtransistor depth neural probes. Nat. Nanotechnol. 17, 301–309 (2022). [PubMed: 34937934]

42. Masvidal-Codina E et al. High-resolution mapping of infraslow cortical brain activity enabled by graphene microtransistors. Nat. Mater. 18, 280–288 (2019). [PubMed: 30598536]

43. Lu Y et al. Ultralow impedance graphene microelectrodes with high optical transparency for simultaneous deep two-photon imaging in transgenic mice. Adv. Funct. Mater. 28, 1800002 (2018). [PubMed: 34084100]

44. Xia J et al. Measurement of the quantum capacitance of graphene. Nat. Nanotechnol 4, 505–509 (2009). [PubMed: 19662012]

45. Liu X et al. Multimodal neural recordings with Neuro-FITM uncover diverse patterns of cortical–hippocampal interactions. Nat. Neurosci. 24, 886–896 (2021). [PubMed: 33875893]

46. Ł ski S et al. Frequency dependence of signal power and spatial reach of the local field potential. PLoS Comput. Biol. 9, e1003137 (2013). [PubMed: 23874180]

47. Myers JC et al. The spatial reach of neuronal coherence and spike-field coupling across the human neocortex. J. Neurosci. 42, 6285–6294 (2022). [PubMed: 35790403]

48. Liu X et al. Decoding ECoG high gamma power from cellular calcium response using transparent graphene microelectrodes. In Proc. 2019 9th International IEEE/EMBS Conference on Neural Engineering (NER) 710–713 (IEEE, 2019).

49. Gallego JA et al. Neural manifolds for the control of movement. Neuron 94, 978–984 (2017). [PubMed: 28595054]

50. Elsayed GF et al. Reorganization between preparatory and movement population responses in motor cortex. Nat. Commun. 7, 13239 (2016). [PubMed: 27807345]

51. Stringer C et al. Spontaneous behaviors drive multidimensional, brainwide activity. Science 364, eaav7893 (2019).

52. Okun M et al. Diverse coupling of neurons to populations in sensory cortex. Nature 521, 511–515 (2015). [PubMed: 25849776]

53. Stringer C et al. High-dimensional geometry of population responses in visual cortex. Nature 571, 361–365 (2019). [PubMed: 31243367]

54. Lin MZ & Schnitzer MJ Genetically encoded indicators of neuronal activity. Nat. Neurosci. 19, 1142–1153 (2016). [PubMed: 27571193]

55. Zhang D et al. Dealing with the foreign-body response to implanted biomaterials: strategies and applications of new materials. Adv. Funct. Mater. 31, 2007226 (2021).

56. Carnicer-Lombarte A et al. Foreign body reaction to implanted biomaterials and its impact in nerve neuroprosthetics. Front. Bioeng. Biotechnol. 9, 271 (2021).

57. Salatino JW et al. Glial responses to implanted electrodes in the brain. Nat. Biomed. Eng. 1, 862–877 (2017). [PubMed: 30505625]

References

58. Wang Y et al. Electrochemical delamination of CVD-grown graphene film: toward the recyclable use of copper catalyst. ACS Nano 5, 9927–9933 (2011). [PubMed: 22034835]

59. Brug G et al. The analysis of electrode impedances complicated by the presence of a constant phase element. J. Electroanal. Chem. Interfacial Electrochem 176, 275–295 (1984).

60. Mayford M et al. Control of memory formation through regulated expression of a CaMKII transgene. Science 274, 1678–1683 (1996). [PubMed: 8939850]

61. Wekselblatt JB et al. Large-scale imaging of cortical dynamics during sensory perception and behavior. J. Neurophysiol. 115, 2852–2866 (2016). [PubMed: 26912600]

62. Mitani A & Komiyama T Real-time processing of two-photon calcium imaging data including lateral motion artifact correction. Front. Neuroinform. 12, 98 (2018). [PubMed: 30618703]

63. Pachitariu M et al. Suite2p: beyond 10,000 neurons with standard two-photon microscopy. Preprint at bioRxiv 10.1101/061507 (2016).

64. Yu BM et al. Gaussian-process factor analysis for low-dimensional single-trial analysis of neural population activity. in Advances in Neural Information Processing Systems Vol. 21 (Curran Associates, 2008).
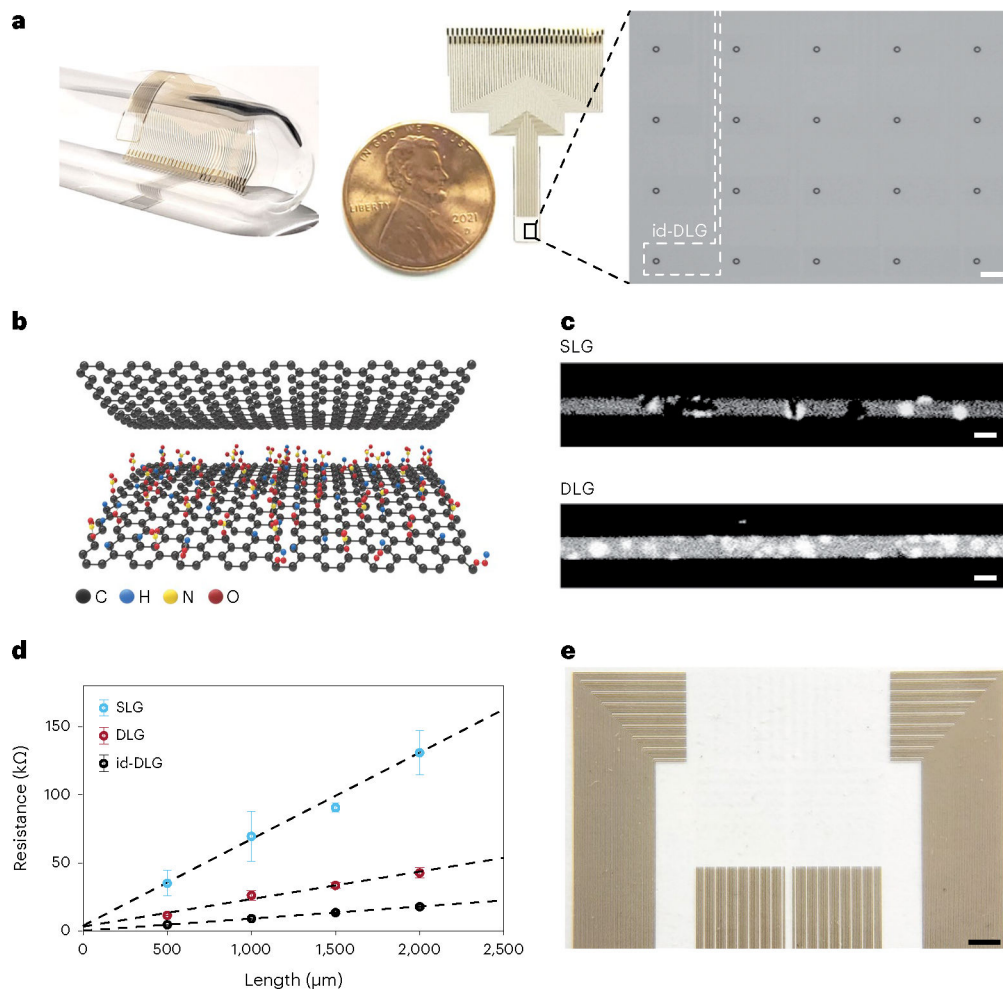
**Fig. 1 |. High-density transparent graphene array.**
a, Transparent and flexible 64-channel graphene array (left) and a magnified part of it with graphene wires shown with white dashed lines (right). Scale bar, 100 μm. **b**, Schematic of HNO$_3$ id-DLG. **c**, Two-photon microscopy image of pinhole defects on the graphene wires. The top and bottom wires are SLG and DLG, respectively. Scale bars, 10 μm. **d**, Graphene wire resistance for SLG, DLG and id-DLG wires as a function of wire length. The circles and error bars indicate the mean and standard deviation, respectively ($n = 4$). **e**, Optical image of high-density 256-channel graphene array. Scale bar, 1 mm.
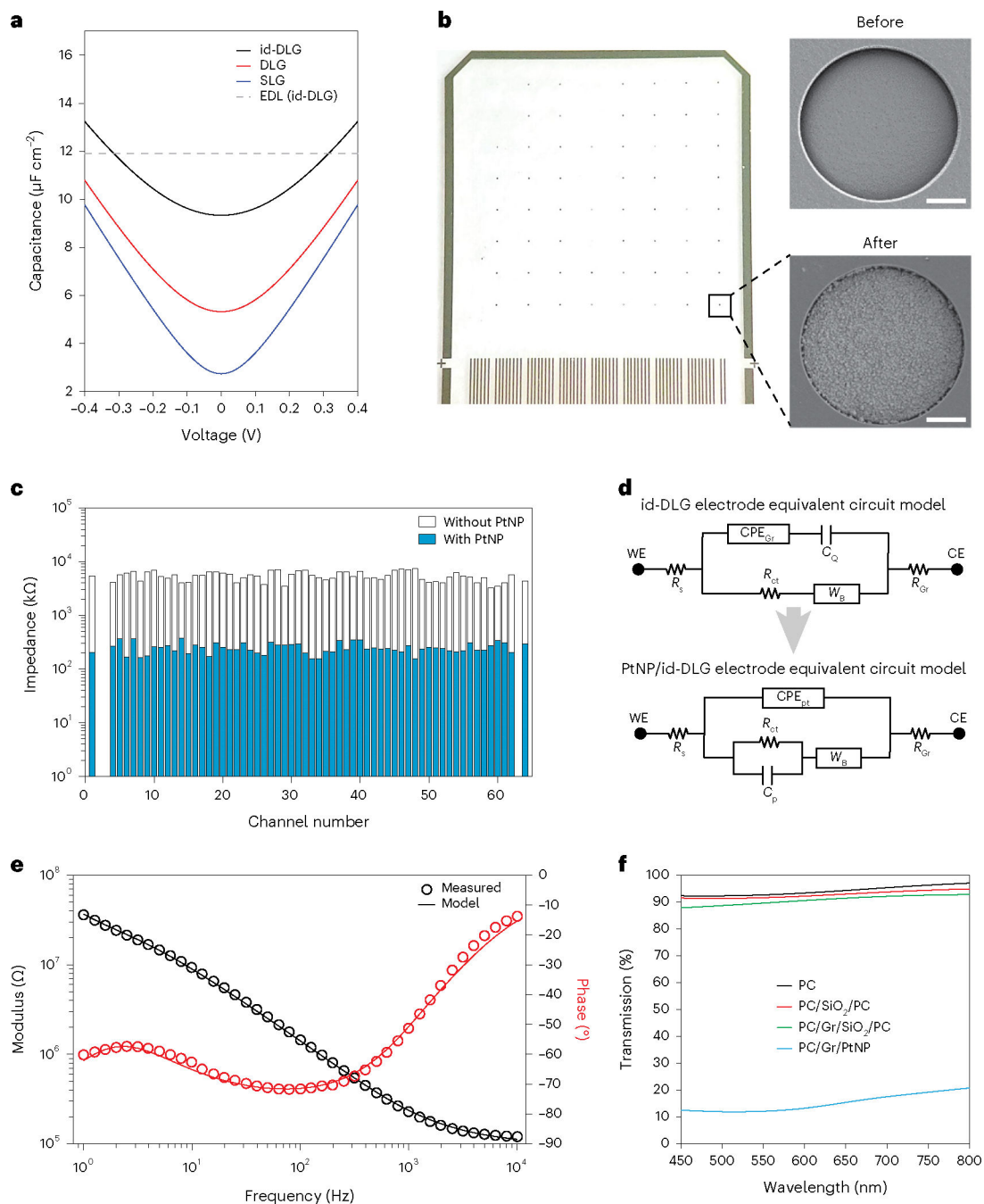
Fig. 2 |. Overcoming quantum capacitance and reducing the impedance with PtNP deposition.
a, Quantum capacitance for SLG, DLG, id-DLG and the Helmholtz electrical double-layer
(EDL) capacitance are plotted as a function of voltage. The quantum capacitance is
dominant in the open-circuit potential range of graphene (−100 to 100 mV). **b**, Optical
image of the 64-channel array (left) and example scanning electron microscopy images
of the electrode openings before and after PtNP deposition (right). Scale bars, 5 μm. **c**,
Impedance distribution of 64 channels at 1 kHz measured before and after PtNP deposition.
The average impedances of the electrodes are 5.4 ± 1.1 MΩ and 250 ± 56 kΩ (mean ±

standard deviation), before and after PtNP deposition, respectively. **d**, Equivalent circuit model for the id-DLG electrode with and without PtNPs. R_s is the solution resistance; R_{Gr} is the graphene wire resistance; C_Q is the quantum capacitance; CPE_{Gr} and CPE_{Pt} are the constant phase elements (CPEs) representing the EDL of id-DLG and PtNP/id-DLG electrodes, respectively. W_B is the bounded Warburg element explaining the diffusion process, and R_{ct} is the charge-transfer resistance that simulates the Faradaic reactions. WE and CE stand for the working electrode and counter electrode, respectively. **e**, Measured EIS data of the PtNP/id-DLG electrode and the fitted values using the equivalent circuit model. **f**, Transmittance of different stacks that constitute the array. PC and Gr stand for parylene C and graphene, respectively.
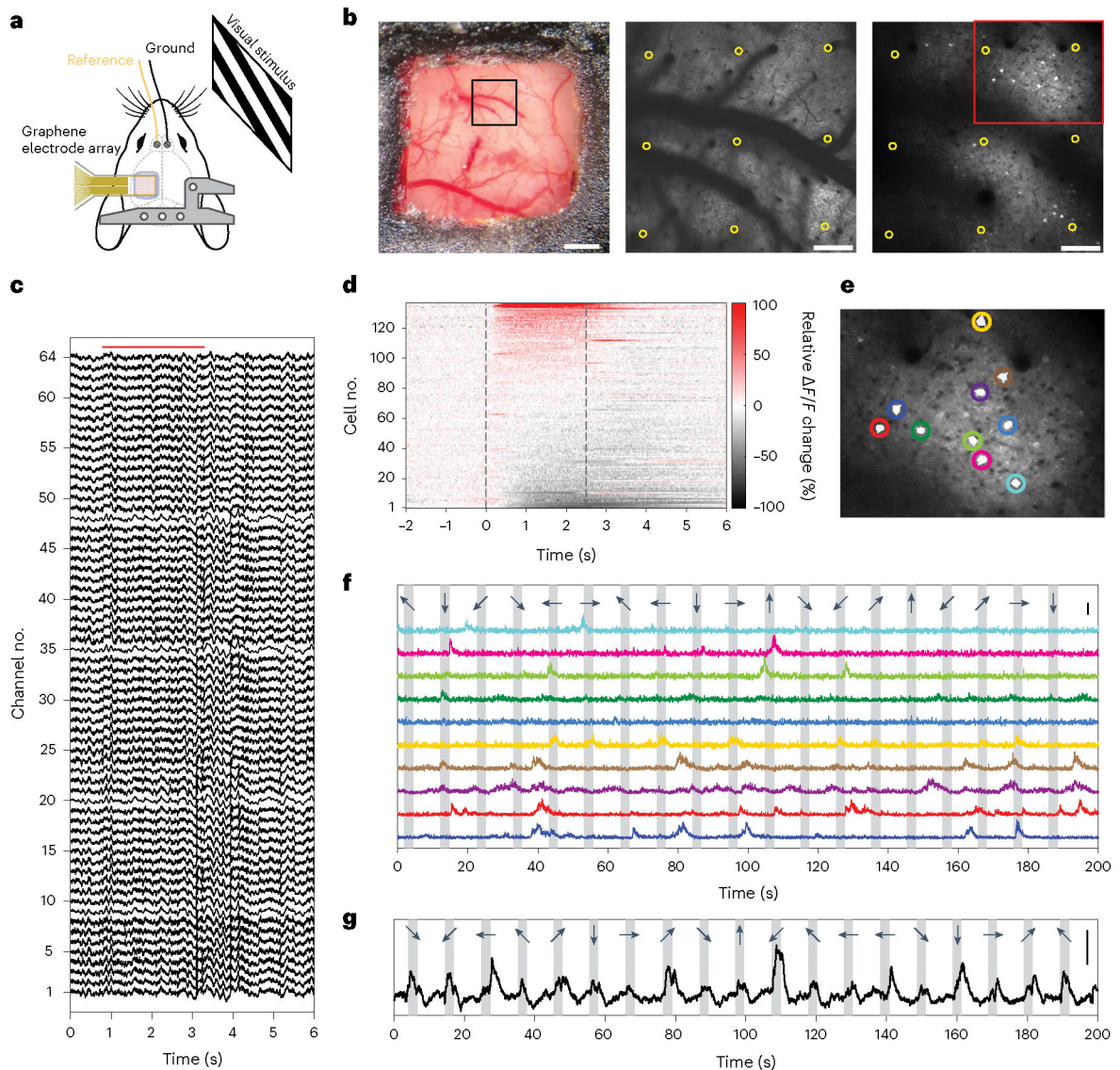
Fig. 3 |. Multimodal experiments combining the recordings of cortical potentials from surface and two-photon imaging at two different depths.

a, Schematic of the multimodal experimental setup. **b**, Exposed cortex area covered by the array with the imaging FoV depicted by the black square (left) and time-averaged two-photon images of L1 (middle) and L2/3 (right). PtNP/id-DLG electrodes are shown by the yellow circles. Scale bars, 700 μm (left) and 150 μm (middle and right). **c**, Representative surface potentials recorded from the 64 channels of the array. The red line shows the duration of visual stimulus. **d**, Trial-averaged population activity (relative to the 2 s baseline before stimulus onset) of neurons detected in L2/3. The black dashed lines show the onset and offset of visual stimuli. **e,f**, Ten neurons highlighted from the red box in **b** (**e**) and their normalized *F*/*F* signals (**f**). **g**, Pixel-level average *F*/*F* signal of L1. Scale bars, 5 *z*-score (**f,g**). The black arrows and grey bars in **f** and **g** show the direction and duration of drifting gratings, respectively.
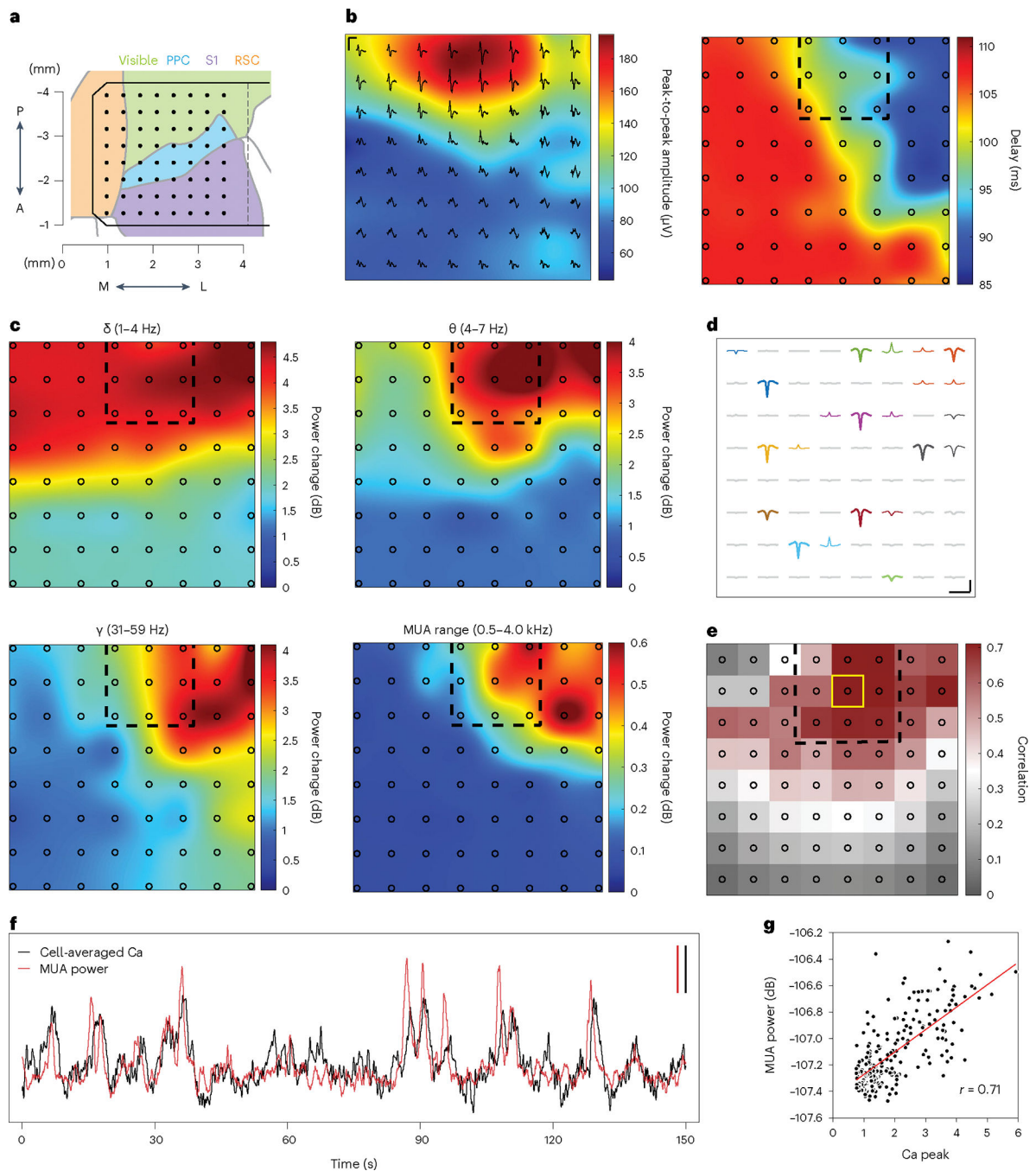
Fig. 4 |. Stimulus-evoked local field potentials and high-frequency activities detected using electrodes on the cortical surface.
**a**, Cortical regions covered by the 64 channels of the array. The total area covered is 2.45×2.45 mm^2. **b**, Peak-to-peak amplitude (left) and delay map (right) of the visually evoked responses. Scale bars, 250 ms (horizontal) and 100 μV (vertical). **c**, Spatial maps of the evoked powers (relative to the baseline) at different frequency bands across the array. High-frequency activities are spatially localized, whereas low-frequency bands have broad propagation ranges. **d**, Representative event-triggered MUA waveforms on different

channels. Scale bars, 2 ms (horizontal) and 20 μV (vertical). If multiple nearby channels also captured the neural events, they were assigned the same colour as the target channel. **e**, Correlation between the cell-averaged calcium peaks and MUA power around the peak onset for all the 64 channels. The channels in the FoV show the highest correlation values. The yellow box shows the channel with the maximum correlation ($r = 0.71$). The black dashed boxes and black circles in the colour maps in **b**, **c** and **e** indicate the FoV and the electrodes' locations, respectively. **f**, Representative cell-averaged F/F and MUA power of the channel with the maximum correlation (yellow box in **e**). The correspondence between the two signals is evident from the sharp deflections in the MUA power followed by the peaks in the calcium signal. Black scale bar, 2 z-score (calcium). Red scale bar, 0.5 dB (MUA power). **g**, Scatter plot of the cell-averaged calcium peaks and the corresponding MUA powers for the channel with the maximum correlation (yellow box in **e**).
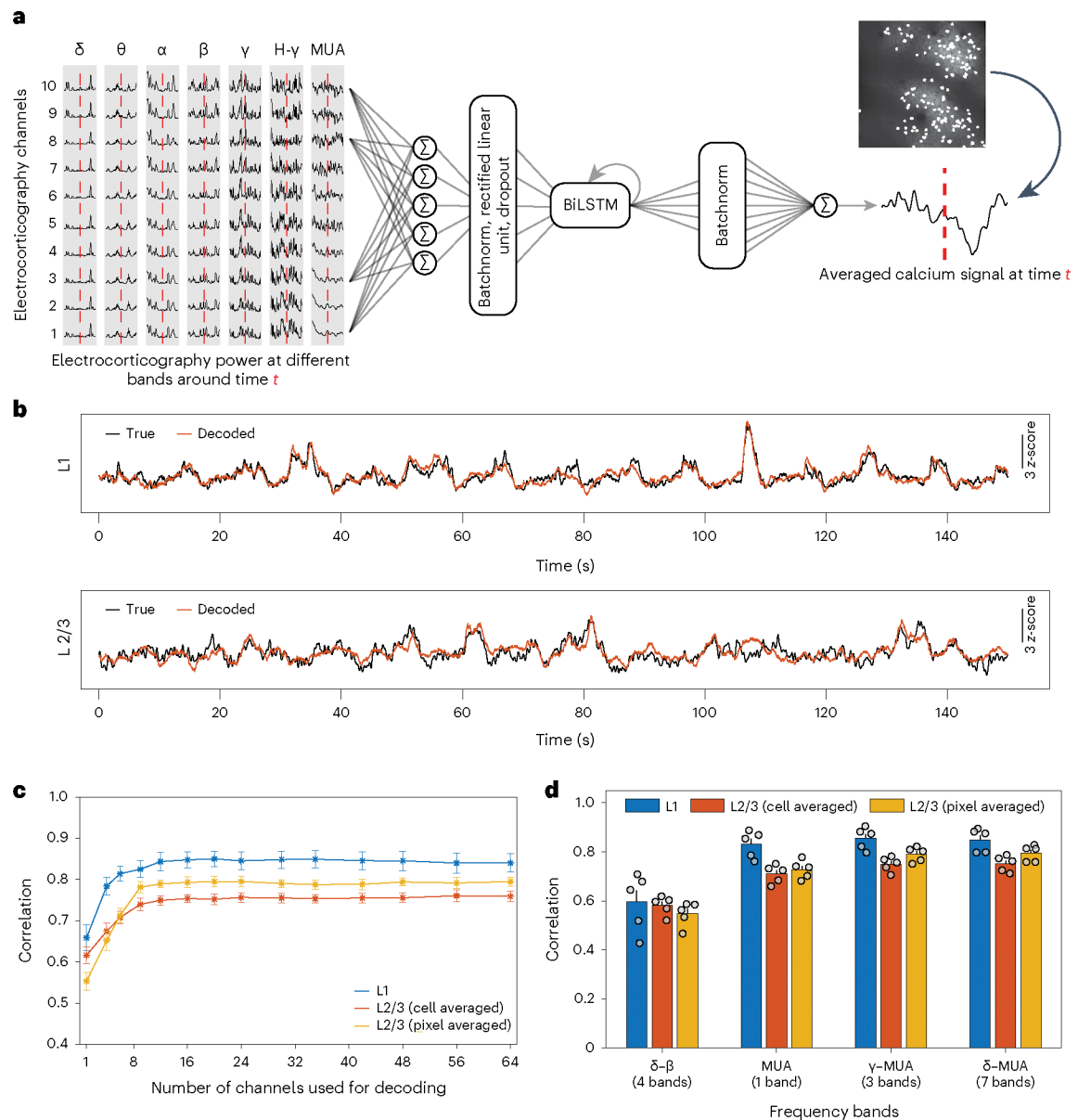
Fig. 5 |. Decoding the average calcium activity from recorded surface potentials.
a, Schematic of the decoding model. The signal powers at different frequency bands (ten channels are shown as an example) around time t are used as inputs to the model to decode the calcium activity at time t. The model consists of a linear hidden layer, a single-layer BiLSTM network and a linear readout layer. **b**, Decoded (orange) versus ground-truth (black) F/F values of L1 (pixel averaged) and L2/3 (cell averaged). **c**, Decoding performances of L1 and L2/3 (cell and pixel averaged) using all the seven frequency bands but different numbers of channels. The circles and error bars indicate the mean and standard error of the mean, respectively ($n = 5$). **d**, Decoding performances of L1 and L2/3 (cell and pixel averaged) using the low-frequency (δ, θ, α and β) and high-frequency (γ, H-γ and MUA) components of the 20 channels closest to the FoV. The bars and black lines indicate the mean and standard error of the mean, respectively ($n = 5$).
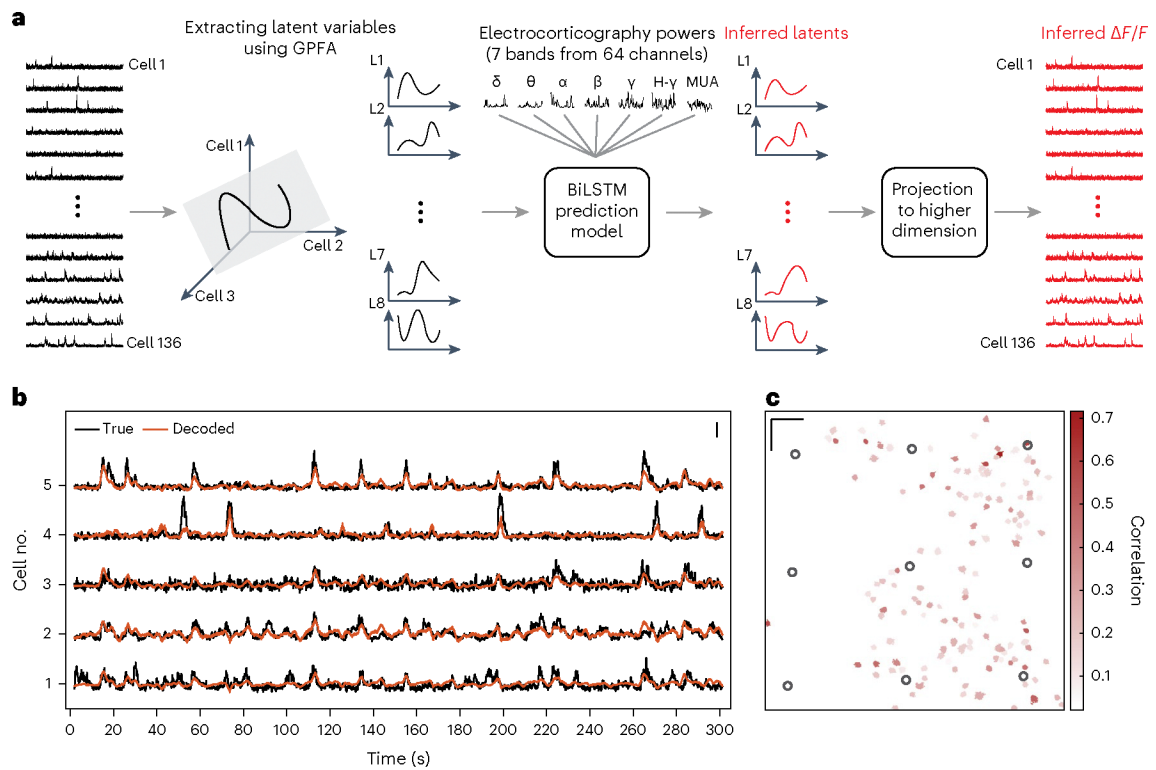
Fig. 6 |. Decoding single-cell calcium activity from surface potentials using latent variables.
a, Schematic of the single-cell decoding model. Eight latent variables (L1 to L8) extracted using GPFA are used to train the BiLSTM models (similar to that shown in Fig. 5a). The inferred latent variables are projected to the high-dimensional space to achieve single-cell F/F signals. **b**, Representative examples for the decoded (orange) versus ground-truth (black) F/F values of the five best-decoded cells. Scale bar, 3 z-score. **c**, Decoding performance for all the 136 cells with their locations outlined in the FoV. The black circles are the nine channels inside the FoV. Scale bars, 100 μm.